Electromagnetic design of the transition section between modules of a wakefield accelerator

A. Siy,[1,2,*] N. Behdad,[1] J. Booske,[1] G. Waldschmidt,[2] and A. Zholents[2,†]

[1]*University of Wisconsin, Madison, Wisconsin 53715, USA*

[2]*Advanced Photon Source, Argonne National Laboratory, Argonne, Illinois 60439, USA*

(Received 2 August 2022; accepted 7 December 2022; published 18 January 2023)

The electromagnetic design of a transition section consisting of couplers for extracting the 180-GHz TM_{01} accelerating mode and 190-GHz HE_{11} dipole mode of a cylindrical corrugated waveguide used as a collinear wakefield accelerator is presented. Extraction of the high power accelerating mode reduces the power dissipation in the corrugated accelerating structure and allows the much weaker HE_{11} mode to be isolated and used to monitor the stability of the 10-nC electron drive bunch. The final design demonstrates wide bandwidth and high coupling efficiency of two couplers. The design was also optimized to have the surface electric and magnetic fields that do not exceed those in the corrugated waveguide. Finally, coupling between the drive electron bunch and the HE_{11} dipole mode in the corrugated waveguide is considered and the utility of the TE_{11} coupler for detecting the electron beam oscillations in the wakefield accelerator is demonstrated using a few representative examples of oscillations below and above a threshold of the beam breakup instability.

DOI: 10.1103/PhysRevAccelBeams.26.012802

I. INTRODUCTION

The Argonne sub-THz accelerator (A-STAR) is a high gradient, high repetition rate collinear wakefield accelerator (CWA) under development at Argonne National Laboratory for use in a future x-ray free electron laser (XFEL) facility [1,2]. A-STAR is based on a corrugated waveguide (CWG) which acts as a slow wave structure, generating a 90 MV m^{-1} accelerating gradient when excited by a 10-nC drive bunch [3]. The accelerating gradient of the wakefield increases the energy of a 150-pC witness electron bunch following close behind the drive bunch to roughly $\mathcal{E}_0(1+\mathcal{R})$, where $\mathcal{E}_0$ is the initial energy of both beams and $\mathcal{R}$ is the transformer ratio, determined by the longitudinal charge density distribution of the drive bunch [4,5]. In A-STAR, $\mathcal{R}=5$ and $\mathcal{E}_0=1$ GeV, resulting in a final witness bunch energy of over 5 GeV. The A-STAR CWA is composed of many 0.5-m long CWG modules placed in series and connected by short interface sections containing electromagnetic couplers, vacuum pumping ports, water cooling outlets, and bellows. The electromagnetic couplers in the interface region extract the TM_{01} accelerating mode and HE_{11} dipole mode from the CWG and will be referred to, in aggregate, as the transition section. The vacuum space of the transition section along with a short section of the CWG accelerating structure is illustrated in Fig. 1. The primary focus of this paper will be the electromagnetic design of the transition section, with details of the thermal loading and expected output signals also being discussed. Additional details regarding the mechanical design are presented in [6].

The wakefield excited by the drive bunch in the CWG is predominantly a TM_{01} mode with a group velocity v_g of $0.57c$ and a peak pulse power of 68 MW. The rf pulse decays exponentially behind the drive bunch due to ohmic loss in the walls of the CWG and has a length of 1.26 ns, determined by the 0.5 m length of the CWG module and the

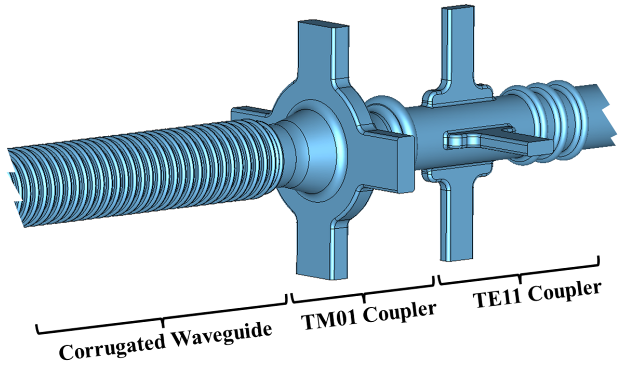

FIG. 1. Vacuum space of transition section couplers connected to a short section of the CWG accelerating structure.

---

[*] asiy@wisc.edu

[†] azholents@anl.gov

group velocity of the traveling wave [3]. Since only a fraction of the electromagnetic energy emitted by the drive bunch is absorbed by the witness bunch, it is desirable to extract the residual energy from the CWG to reduce the overall thermal load on subsequent structures. The TM_{01} coupler in the transition section serves this purpose by removing the unused energy which would otherwise be dissipated as heat in the CWG.

In addition to the TM_{01} mode, the HE_{11} mode is present in the CWG when electrons in the drive bunch propagate off-axis. The transverse momentum kick generated by the HE_{11} mode is responsible for causing a beam breakup (BBU) instability where the tail of the drive bunch is deflected into the accelerator wall [7–9]. Preventing BBU requires precision alignment of the bunch's trajectory with the center axis of the CWG to minimize excitation of the HE_{11} mode. The magnitude of the HE_{11} mode in each accelerating module can be monitored to indicate whether the trajectory is sufficiently aligned to prevent the onset of BBU. Since the HE_{11} mode in the CWG converts primarily to a TE_{11} mode as it propagates to the cylindrical waveguide input of the transition section, we include a TE_{11} coupler, referred to as the integrated offset monitor (IOM), to measure the power in the HE_{11} mode originating from the CWG. Integrating the rf power output from the IOM with a bolometer provides an effective measure of the drive bunch's stability which we will demonstrate in Sec. IV.

II. ELECTROMAGNETIC DESIGN

The electromagnetic design of the transition section output couplers began by considering the structures proposed in [10] and [11]. Modifications were made to the designs in the literature to reduce peak fields and increase bandwidth. Wide coupling bandwidth was desired to accommodate manufacturing tolerances of the CWG which shifts its synchronous TM_{01} center frequency by roughly 1 GHz/μm of error in corrugation depth. Minimization of the peak surface fields to levels below those in the CWG was also desired to limit rf breakdown from the 68-MW, 1.26-nS incident pulse. The final design of the transition section is illustrated in Fig. 2, showing the TM_{01} and TE_{11} couplers in series.

Because the circular waveguide input of the transition section is overmoded at the 180-GHz operating frequency, mode conversion presented a significant design challenge. One approach to eliminating conversion to higher modes is to taper the circular waveguide input to a narrower diameter that only supports the lowest order TE and TM modes at the operating frequency. This approach is undesirable since it requires additional length and increases the peak fields and associated thermal load on the structure, among other factors. A second, more desirable approach, is to use a symmetric structure that only supports modes with the same symmetry as the coupler geometry. This approach was used to preserve the 2-mm inner diameter of the transition section while eliminating coupling to higher modes. As illustrated in Fig. 3, the TM_{01} coupler has two perfect magnetic conductors (PMC) symmetry planes when excited by the TM_{01} mode. The twofold PMC symmetry allows only $TM_{2i,n}$ type modes to exist, where i and n are integers ranging from 0,1,2... and 1,2,3..., respectively. In the symmetric structure, the next accessible mode above TM_{01} is TM_{21} which is cut off and unable to propagate at the 180-GHz input frequency from the CWG. A final advantage of the symmetric output coupler is a reduction of peak surface fields due to multiple waveguide outputs reducing the overall power density in the structure.

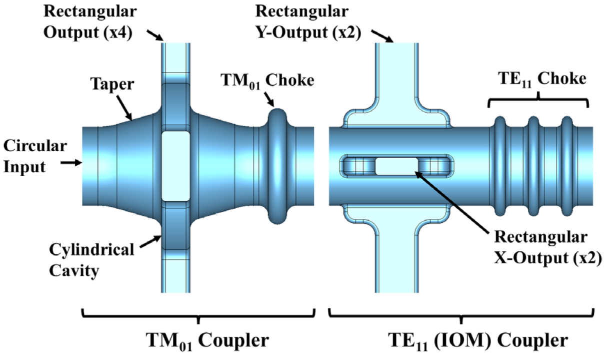

FIG. 2. Vacuum space of the TM_{01} and TE_{11} couplers in the transition section.

As illustrated in Fig. 2, the TM_{01} coupler consists of a four-way rectangular waveguide cross, connected to a cylindrical waveguide via tapers and a circular cavity. Immediately following the waveguide cross is an rf choke which reflects the TM_{01} mode. When the incident TM_{01} wave encounters the coupler cross, a portion is transmitted to the choke where it is reflected back through the coupler cross with a phase shift. The length of the spacer between the choke and coupler cross is chosen such that the phase shifted wave perfectly cancels the initially reflected wave incident on the coupler cross. Under this condition, nearly

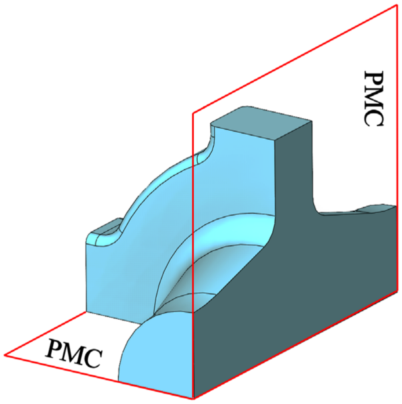

FIG. 3. Vacuum space of a quarter section of the coupler cross, showing the two PMC symmetry planes used to eliminate higher modes in the overmoded cylindrical waveguide.

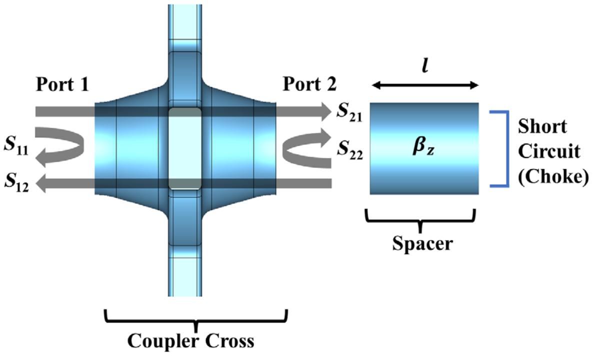

FIG. 4. Schematic of the simplified TM_{01} coupler optimization scheme, showing the coupler cross isolated from the idealized rf choke.

all of the incident power exits through the rectangular waveguide outputs.

The coupler geometry was modeled parametrically in CST Microwave Studio [12] and parameter sweeps were used to optimize the model dimensions. To simplify optimization, the rf choke was idealized as a perfectly reflecting short circuit, as shown in Fig. 4, and the effective reflection coefficient S_{11}^{eff} of the idealized configuration was calculated as

$$S_{11}^{\mathrm{eff}} = S_{11} - \frac{S_{12}S_{21}}{S_{22} + e^{2j\beta_z l}}, \tag{1}$$

where the S-parameters were obtained by simulation of the coupler cross alone. Setting S_{11}^{eff} to zero at the 180-GHz center frequency produces the required spacer length l_0:

$$l_0 = \frac{1}{2\beta_{z0}} \arg\left(\frac{S_{12}S_{21}}{S_{11}} - S_{22}\right), \tag{2}$$

where the arg function returns the phase of its complex argument and β_{z0} is the propagation constant of the 180-GHz TM_{01} mode in the 2-mm diameter circular waveguide. Inserting l_0 back into Eq. (1) produces S_{11}^{eff} as a function of frequency which serves as an objective function for minimization over the desired bandwidth. Using the idealized optimization configuration in Fig. 4 greatly reduces computation time by removing the spacer and choke from the simulation geometry. After the coupler cross was optimized in isolation, the choke and spacer were added to the simulation and a sweep of the spacer length was conducted to find the final geometry.

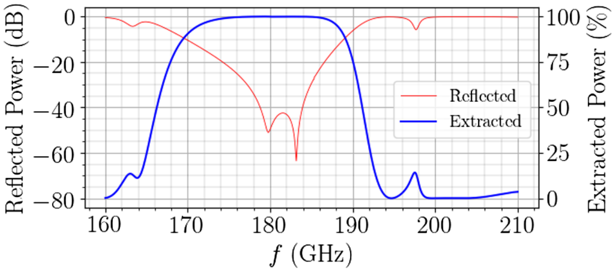

FIG. 5. Reflection and extraction of the TM_{01} mode from the TM_{01} coupler. The extracted power is divided equally among the four rectangular waveguide outputs.

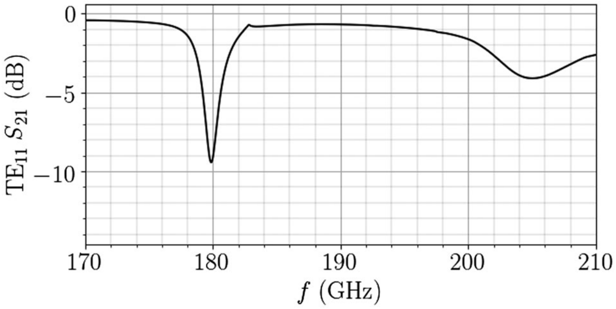

FIG. 6. Transmission of the TE_{11} mode through the TM_{01} output coupler.

rf characteristics of the optimized TM_{01} coupler are illustrated in Fig. 5. The TM_{01} mode coupling efficiency at 180 GHz is 99.1% with 3-dB bandwidth of 25 GHz. Since the TM_{01} coupler must remain transparent to the TE_{11} mode, TE_{11} transmission through the coupler cross was used as a secondary objective function to be maximized around the 190-GHz center frequency of the IOM. TE_{11} transmission of −0.68 dB or 86% through the TM_{01} coupler is shown in Fig. 6.

The design of the TE_{11} coupler for the IOM followed a similar approach to the TM_{01} coupler, with the simplification that only a single objective function was needed in the optimization. The design has two pairs of orthogonal rectangular waveguide outputs corresponding to the two polarizations of the TE_{11} mode, as shown in Fig. 2. The broadwalls of the rectangular waveguide outputs were stepped to a wider dimension at the interface to the circular waveguide to improve coupling efficiency and the short walls were kept narrow to reduce local wakefield power induced by the drive bunch passing through the structure. The rf characteristics of the IOM in isolation are shown in

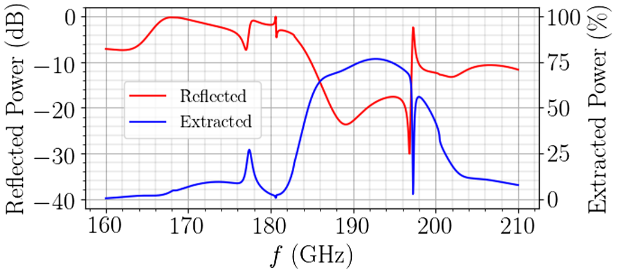

FIG. 7. Reflection and extraction of the TE_{11} mode from the IOM in isolation. The extracted power is divided between the two rectangular waveguide outputs corresponding to the polarization of the incident TE_{11} mode.

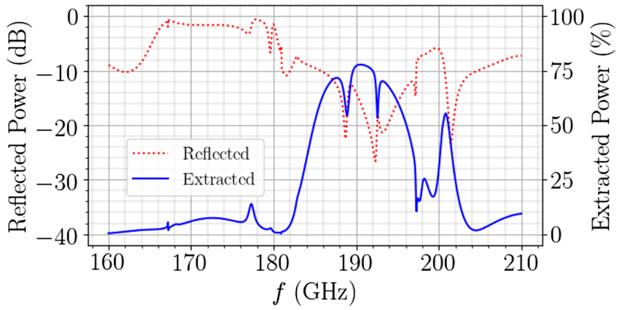

FIG. 8. TE_{11} extraction and reflection from the transition section including the TM_{01} coupler before the IOM.

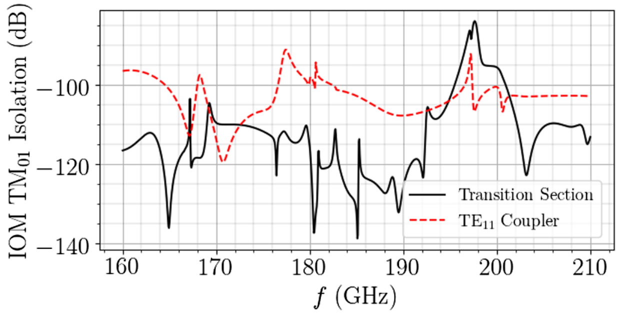

FIG. 9. Isolation of the IOM output from the high power TM_{01} accelerating mode for the TE_{11} IOM coupler alone and for the transition section.

Fig. 7. The extracted power is 73.4% at 190 GHz with a 3-dB bandwidth of approximately 16 GHz.

Combining the TM_{01} and TE_{11} output couplers in series results in the complete transition section geometry shown in Fig. 2. The TM_{01} coupler distorts the TE_{11} response as shown in Fig. 8 which shows the TE_{11} coupling efficiency of the entire structure. The resonances in the passband are caused by a standing wave in the spacer between the two couplers. The spacer's length was selected to position these resonances at an equal distance from 190 GHz. In addition to high coupling efficiency for the TE_{11} mode, a key requirement for the transition section is the isolation of the IOM output from the 180-GHz TM_{01} accelerating mode. Figure 9 shows the TM_{01} isolation for the complete transition section as well as for the stand-alone IOM. The inclusion of the TM_{01} coupler before the IOM increases isolation by roughly 10 dB, to better than −110 dB across the TM_{01} coupling band from 170–190 GHz, as well as reduces thermal loading and peak fields in the IOM.

III. PEAK FIELDS AND THERMAL POWER DISSIPATION

The peak electromagnetic surface fields, transient pulse heating, and steady-state thermal power dissipation all pose limitations on the operation of the transition section. As a design goal, we require the peak surface fields inside the transition section to remain below those in Table I for the CWG, so as not to limit the accelerating gradient of the overall CWA. The pulsed power in the TM_{01} mode due to a single bunch at the end of the CWG of length L is [3]:

$$P_p(t) = \frac{E_{\mathrm{acc}}^2 v_g}{4\kappa(1-\beta_g)} e^{\frac{-2\alpha v_g t}{1-\beta_g}} \Pi\left(\frac{v_g t}{L(1-\beta_g)} - \frac{1}{2}\right), \tag{3}$$

where $\Pi(x)$ is the rectangular window function

$$\Pi(x) = \begin{cases} 1 & |x| < 1/2 \\ 0 & \text{else} \end{cases}, \tag{4}$$

$E_{\mathrm{acc}} = 2\kappa q_0 |F|$ is the accelerating field gradient in the CWG [3], κ is the wakefield loss factor, q_0 is the drive bunch charge, F is the form factor, $v_g = c\beta_g$ is the group velocity, and α is the attenuation constant in $\mathrm{Np\,m^{-1}}$. Values of the relevant parameters are given in Tables I and II and lead to a peak pulse power of 68 MW which decays exponentially with a time constant of $\tau_i = 0.54$ ns, as shown in Fig. 10.

TABLE I. A-STAR CWG operating parameters.

	TM_{01}	HE_{11}	Units
E_{acc}	90	...	$\mathrm{MV\,m^{-1}}$
E_{max}	325	...	$\mathrm{MV\,m^{-1}}$
H_{max}	610	...	$\mathrm{kA\,m^{-1}}$
f	180	190	GHz
κ	1.18×10^{16}	...	$\mathrm{V\,C^{-1}\,m^{-1}}$
$\hat{\kappa}_1$	...	2.19×10^{10}	$\mathrm{V\,C^{-1}\,m^{-1}\,\mu m^{-2}}$
β_g	0.57	0.62	None
α	2.31	1.96	$\mathrm{Np\,m^{-1}}$

The loss factor $\hat{\kappa}_1$ for the HE_{11} mode scales with the square of the beam offset, measured in μm here. The attenuation coefficient α is given for an estimated reduced copper conductivity of $\sigma = 4 \times 10^7\ \mathrm{S\,m^{-1}}$ to account for surface roughness and material properties of the electroformed structure.

TABLE II. A-STAR transition section operating parameters.

Parameter		
q_0	10 nC	Drive bunch charge
f_r	20 kHz	Drive bunch repetition rate
$E_{i,\mathrm{max}}$	210 $\mathrm{MV\,m^{-1}}$	Peak incident surface E-field
$H_{i,\mathrm{max}}$	448 $\mathrm{kA\,m^{-1}}$	Peak incident surface H-field
τ_i	0.54 ns	Incident power time constant
f_i	180 GHz	Incident power frequency
P_i	670 W	Steady-state incident power
$E_{t,\mathrm{max}}$	134 $\mathrm{MV\,m^{-1}}$	Peak trapped surface E-field
$H_{t,\mathrm{max}}$	509 $\mathrm{kA\,m^{-1}}$	Peak trapped surface H-field
τ_t	4.75 ns	Trapped power time constant
f_t	55 GHz	Trapped power frequency
P_t	7.93 W	Steady-state trapped power
P_d	6.07 W	Locally dissipated steady-state incident power
ΔT_{max}	10.9 °C	Maximum temperature rise
L	0.5 m	Length of CWG module

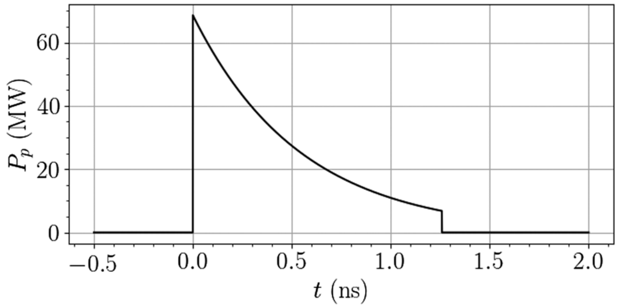

FIG. 10. Power envelope of the incident TM_{01} mode from the output of the 0.5-m long CWG. Calculated with an estimated reduced copper conductivity of $\sigma = 4 \times 10^7\ \mathrm{S\,m^{-1}}$.

Integration of Eq. (3) and multiplication by the bunch repetition rate f_r gives the steady-state TM_{01} power incident on the transition section as

$$P_i = \frac{f_r E_{\mathrm{acc}}^2}{8\kappa\alpha}(1 - e^{-2\alpha L}), \tag{5}$$

which results in 670 W for a 20-kHz bunch repetition rate beam. The peak surface fields produced by the TM_{01} rf pulse are shown in Fig. 11 which shows the maximum E and H fields that occur at the interface of the rectangular waveguide to the tapered cylindrical waveguide.

In addition to the fields of the incident TM_{01} mode, the transition section contains fields directly induced by the electron bunch as it propagates through the structure. The majority of the power coupled directly into the structure is contained in a 55-GHz trapped mode which is seen by observing the wakefield impedance of the structure in Fig. 12. The power dissipated by the trapped mode is calculated as [3]:

$$P_t = f_r \kappa_t q_0^2 |F_t|^2, \tag{6}$$

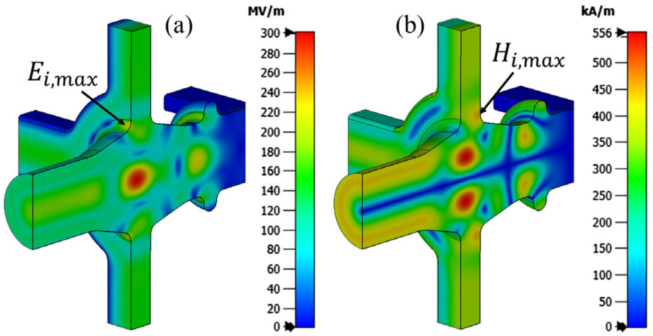

FIG. 11. Maximum E-field (a) and H-field (b) for the incident TM_{01} mode from the CWG with 68 MW peak pulse power. Showing $E_{i,\mathrm{max}} = 210\ \mathrm{MV\,m^{-1}}$ and $H_{i,\mathrm{max}} = 448\ \mathrm{kA\,m^{-1}}$.

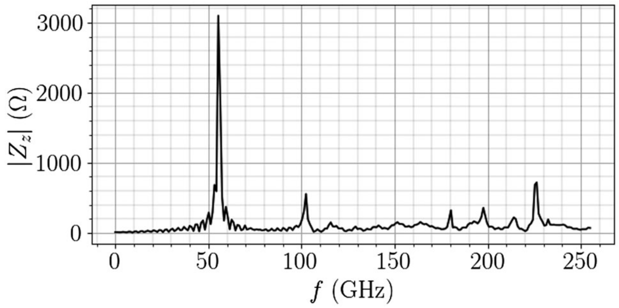

FIG. 12. The z component of the transition section wakefield impedance showing interaction with the trapped mode at 55 GHz.

where f_r is the bunch repetition rate, κ_t is the wakefield loss factor of the trapped mode, q_0 is the drive bunch charge, and F_t is the drive bunch form factor evaluated at the trapped mode frequency. The wakefield loss factor is calculated from the longitudinal electric field of the eigenmode solution as

$$\kappa_t = \frac{1}{4U}\left|\int_0^{L_t} E_z(z) e^{jk_t z} dz\right|^2, \tag{7}$$

where U is the stored energy, L_t is the length of the transition section, and $k_t = \omega_t / c$ is the wave number of the trapped mode with angular frequency ω_t. Evaluating κ_t from the eigenmode simulation result yields $\kappa_t = 4.82\ \mathrm{V\,pC^{-1}}$. The CWG is driven by a doorstep-type charge distribution [4] which has a form factor [3]:

$$\begin{aligned}|F(k)| = \frac{2k_0}{\mathcal{R}^2 + \pi - 2}\Bigg\{\frac{\mathcal{R}^2}{k^2} + \frac{2k_0}{k^3}\Bigg[\frac{k_0}{k} \\ \times\left[1 - \cos\left(kl - \frac{\pi k}{2k_0}\right)\right] + \sin(kl) - \sin\left(\frac{\pi k}{2k_0}\right)\Bigg] \\ - \frac{2}{k^2}\sqrt{\mathcal{R}^2 - 1}\left[\cos(kl) + \frac{k_0}{k}\sin\left(kl - \frac{\pi k}{2k_0}\right)\right]\Bigg\}^{1/2},\end{aligned} \tag{8}$$

where $\mathcal{R}$ is the transformer ratio of the bunch, $k_0 = \omega_0 / c$, ω_0 is the angular frequency of the synchronous TM_{01} accelerating mode in the CWG, and l is the length of the drive bunch given by

$$l = \frac{\frac{\pi}{2} + \sqrt{\mathcal{R}^2 - 1} - 1}{k_0}. \tag{9}$$

Evaluating the form factor for $\mathcal{R} = 5$ at the trapped mode frequency of 55 GHz yields $|F_t| = 0.907$. The power dissipated by a beam with 20 kHz bunch repetition rate and $q_0 = 10$ nC is then calculated from Eq. (6) as 7.93 W. The peak fields of the trapped mode are shown in Fig. 13 which shows the trapped mode peak fields of 134 $\mathrm{MV\,m^{-1}}$ and 509 $\mathrm{kA\,m^{-1}}$ are similar in magnitude to those of the incident rf pulse. The quality factor Q of the trapped mode is

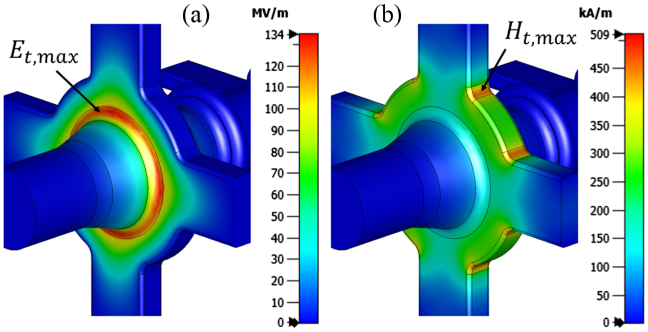

FIG. 13. Peak E-field (a) and H-field (b) of the trapped mode at 55 GHz, excited by a 10-nC bunch.

1.656×10^3, leading to a power decay time constant of $\tau_t = 4.75$ ns.

Combining the steady-state heat load from the incident rf pulse and the trapped mode results in the total power dissipation density shown in Fig. 14. The heat load is concentrated in the cylindrical TM_{01} coupler cavity where the typical thermal load, shown at location (a), is 30 $\mathrm{W\,cm^{-2}}$. The thermal load peaks at location (b), where it reaches 85 $\mathrm{W\,cm^{-2}}$. The total combined heat load on the transition section is 14 W which is composed of 7.93 W from the trapped mode and locally dissipated power of 6.07 W from the 20-kHz incident rf pulse train. The rest of the steady-state incidence power P_i splits between the four TM_{01} waveguides and propagates to the loads passing a set of diamond windows on the way [13].

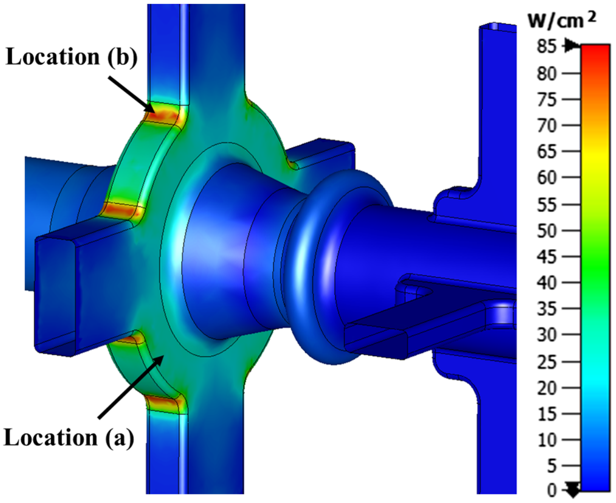

FIG. 14. Steady-state heat load resulting from the 670-W TM_{01} incident rf power and the 55-GHz trapped mode for a 20-kHz repetition rate beam.

The transient temperature rise due to pulse heating of the surface is a contributing factor to the initiation of rf breakdown and should be minimized [14]. The temperature rise is calculated from the tangential surface magnetic field $H_{||}$ which decays exponentially with the skin depth $\delta = 1/\sqrt{\pi f \mu \sigma}$ in the copper wall material. Using the Green's function solution to the heat flow equation with a Neumann boundary condition at the surface results in the following equation for the surface temperature rise [15]:

$$\Delta T(t) = \frac{2}{\rho c_\epsilon}\int_0^t \frac{dP_d}{dA}\frac{1}{\delta}\exp\left[\frac{4\alpha_d(t-t')}{\delta^2}\right] \times \mathrm{erfc}\left[\frac{2}{\delta}\sqrt{\alpha_d(t-t')}\right] dt', \tag{10}$$

where ρ is the material density, c_ϵ is the specific heat, $\alpha_d = k_T/\rho c_\epsilon$ is the thermal diffusivity, k_T is the thermal conductivity, and dP_d/dA is the power dissipation density at the surface. Separating the power dissipation density into components from the trapped mode and the incident rf pulse train yields

$$\frac{dP_d}{dA} = \frac{1}{2}R_{s,t}|H_{||,t}|^2 e^{-t/\tau_t} + \frac{1}{2}R_{s,i}|H_{||,i}|^2 e^{-t/\tau_i} \tag{11}$$

where $R_s = \sqrt{\pi f \mu/\sigma}$ is the surface resistance, f is the frequency, $H_{||}$ is the maximum tangential magnetic field, and τ is the power decay time constant. Observation of Fig. 14 indicates the maximum pulse heating occurs at location (b), where the corners of the rectangular waveguide outputs join the cylindrical cavity of the TM_{01} coupler. At this location, the incident TM_{01} pulse has a peak magnetic field of $H_{||,i} = 425\ \mathrm{kA\,m^{-1}}$ with a decay time constant of $\tau_i = 0.54$ ns and the trapped mode has a peak field of $H_{||,t} = 509\ \mathrm{kA\,m^{-1}}$ with a decay time constant of $\tau_t = 4.75$ ns. Using these values in Eq. (10) and computing the integral numerically produces the transient surface temperature shown in Fig. 15. The maximum temperature rise of 10.9 °C is well below the 40 °C damage threshold cited in the literature [15] and similar to the 9.5-K temperature rise in the CWG [3].

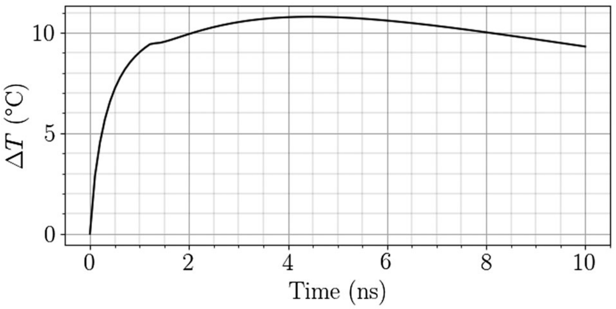

FIG. 15. Transient surface temperature rise at location (b) of Fig. 14, showing a maximum of $\Delta T = 10.9$ °C occurring 4.5 ns from the beginning of the pulse. Computed for a structure with electrical conductivity of $4 \times 10^7\ \mathrm{S\,m^{-1}}$, $k_T = 398\ \mathrm{W\,m^{-1}\,K^{-1}}$, $\rho = 8.9\ \mathrm{g\,cm^{-3}}$, $c_\epsilon = 389\ \mathrm{J\,kg^{-1}\,K^{-1}}$.

IV. IOM SIGNAL

Stable operation of the CWA requires measurement of the drive bunch trajectory to ensure propagation along the central axis of the CWG. When electrons in the drive bunch deviate from the axis, a transverse wakefield is created which imparts a momentum kick on the tail of the bunch, leading to beam breakup (BBU) instability and potential loss of the bunch [7–9]. Here, we propose a technique for measuring the approximate radial offset of particles in the drive bunch using the HE_{11} mode of the CWG which is excited by the off-axis particles.

Following the derivation in Appendix, the form factor of the bunch is modified to account for the HE_{11} E-field's dependence on the radial and azimuthal coordinates r and ϕ. For simplicity, we treat only the x-polarization and approximate the continuous current distribution J_z of the bunch as a delta function such that the modified form factor of Eq. (A14) becomes

$$G_1(t) = \frac{1}{q_0}\int_{-\infty}^{\infty} i(t')x(t',t)e^{-j\omega t'}dt'. \tag{12}$$

Here, q_0 is the drive bunch charge, $i(t')$ is the peak current distribution, ω is the synchronous frequency of the HE_{11} mode, and $x(t',t)$ is the x offset of particles in the bunch, which depends on both the time coordinate within the bunch t' and the global position of the bunch in the CWG described by t. Using the modified form factor, the field amplitude of the HE_{11} mode at the end of the CWG of length L follows the same calculation procedure as Eq. (3):

$$P_{\mathrm{out}}^{1/2}(t) = \sqrt{\frac{2\hat{\kappa}_1 q_0^2|G_1(t_r)|^2 v_g}{1-\beta_g}}e^{\frac{-\alpha(v_g t-\beta_g L)}{1-\beta_g}} \times \cos\left(\omega\left[t-\frac{L}{c}\right]\right)\Pi\left(\frac{2v_g t - L(1+\beta_g)}{2L(1-\beta_g)}\right), \tag{13}$$

where $\hat{\kappa}_1$, α, ω, and β_g are the parameters of the HE_{11} mode given in Table I, and $G_1(t_r)$ is the modified form factor evaluated at the delayed time of the bunch:

$$t_r(t) = \frac{L - v_g t}{c(1-\beta_g)}. \tag{14}$$

When the HE_{11} mode passes from the CWG into the smooth cylindrical waveguide at the input of the transition section, roughly 90% of the power converts to the TE_{11} mode and 10% to the TM_{11} mode of the circular waveguide. Extracting the TE_{11} mode with the TE_{11} IOM coupler and integrating the rf power with a bolometer yields a measurement of the total HE_{11} mode energy excited by the bunch. This energy scales approximately with the integrated radial offset of the particles in the bunch and is indicative of the overall stability of the bunch within the CWG module.

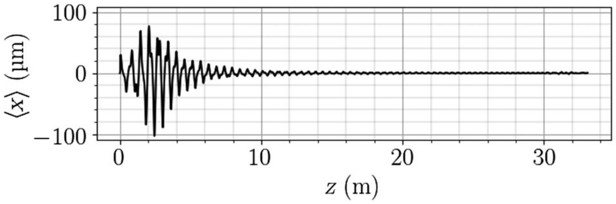

FIG. 16. Radial offset of the drive bunch center of charge propagating through the CWA.

An example drive bunch trajectory through the CWA is shown in Fig. 16. Here, the trajectory is calculated for a drive bunch with an initial offset of 30 μm from the center axis. The initial offset of the bunch causes oscillation of the center of charge as the bunch propagates through the continuous channel of focusing and defocusing quadrupoles surrounding the CWG. The bunch is injected with an energy chirp which leads to BNS damping and eventual stabilization [16,17], as shown in Fig. 16.

A close-up view of the center of charge trajectory between 2 and 2.5 m, corresponding to the fifth 0.5-m long CWG module, is shown in the top panel of Fig. 17. Snapshots of the bunch curvature at three locations in the module are shown in the middle panel, where the tail of the bunch is seen to oscillate about the center axis with a

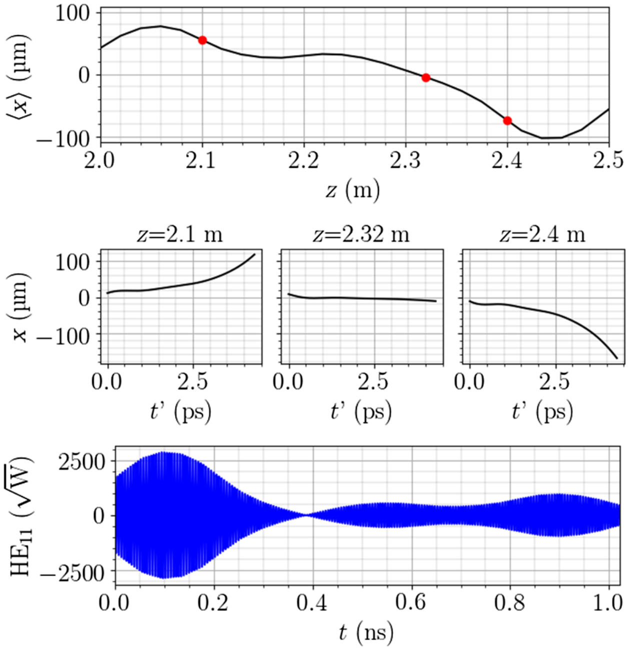

FIG. 17. Bunch trajectory through the fifth 0.5-m long CWG module in the CWA showing the center of charge of the electron bunch (top panel), the bunch curvature at three locations in the CWG (middle panel), and the 190-GHz HE_{11} mode at the end of the CWG module.

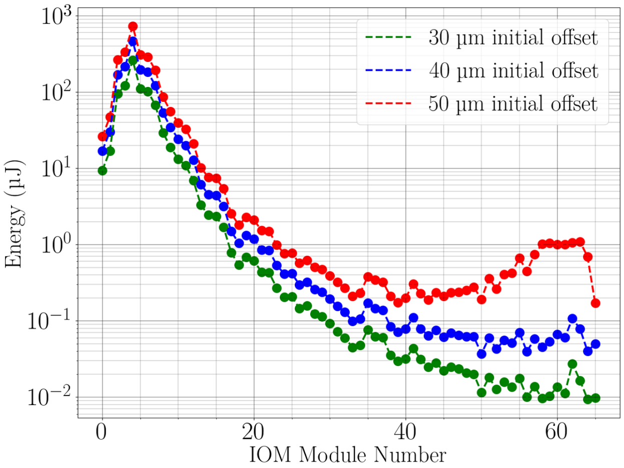

FIG. 18. IOM output energies for bunch trajectories with 30, 40, and 50 μm initial offsets, showing instability developing for the 50-μm initial offset case after module number 40.

greater amplitude than the head. The bottom panel shows the HE_{11} mode amplitude at the end of the CWG module generated by the off-axis particles of the bunch and calculated from Eq. (13). The envelope of the HE_{11} pulse correlates with the bunch offset in the top panel, where the signal at 1.02 ns is generated by the bunch at $z = 2$ m and is attenuated due to ohmic loss in the CWG.

Repeating the HE_{11} signal calculation for each CWG module in the CWA and applying the HE_{11} to the TE_{11} conversion efficiency of 90% and IOM coupling efficiency for a single waveguide output of 35%, as shown in Fig. 8, results in the total integrated energy from each IOM shown in Fig. 18. Here, the 30-μm initial offset case corresponds to the trajectory shown in Fig. 16 where the bunch is stabilized over the length of the CWA. Increasing the initial bunch offset to 50 μm results in a growing instability of the bunch at the end of the CWA, as shown by the increasing IOM energy output. In the second numerical example, one quadrupole located in the accelerator module 28 was misaligned by 5, 6, and 7 μm. Figure 19 shows the total energy intercepted by each IOM behind the quadrupole. Stable operating conditions of the CWA are estimated to require initial bunch offsets of less than 40 μm and quadrupole misalignment errors of less than 6 μm. Therefore, given the magnitude of the calculated IOM output energies, the IOMs are expected to inform about the unwanted beam oscillation in the accelerator much before the onset of the BBU instability.

In addition to the HE_{11} signal generated by the off-axis particles in the drive bunch, the IOM emits a baseline signal induced by the bunch interacting with the TE_{11} coupler as it propagates through the transition section. The total baseline energy for a 10-nC door-step [4] distribution drive bunch with a transformer ratio of 5 and 100 μm, vertical offset is simulated to be 2.06 μJ per waveguide output in the horizontal plane and 1.85 μJ per waveguide output in the vertical plane. The baseline signal is distributed over many modes of the rectangular waveguide. Figure 20 shows the baseline energy in the first 20 waveguide modes. Limiting the energy in the baseline signal reduces the dynamic range required to accurately measure the HE_{11} signal. Since the desired signal is contained in the fundamental TE_{10} mode of the rectangular waveguide, a linear polarizer placed in front of the IOM waveguide output can limit the baseline signal contained in the cross-polarized modes. Frequency filtering can also be explored to reduce the baseline energy which has the spectrum shown in Fig. 21 where the majority of the energy is above 350 GHz.

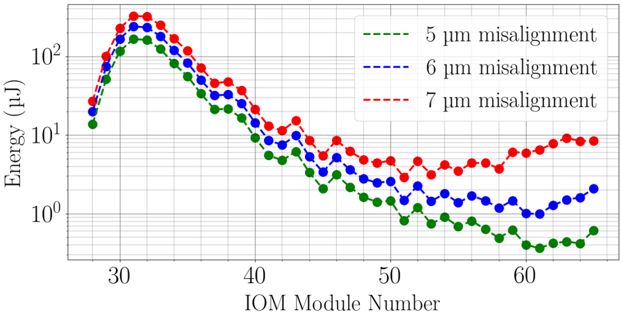

FIG. 19. IOM output energies for one quadrupole misalignment of 5, 6, and 7 μm, showing instability developing for the 7-μm misalignment case.

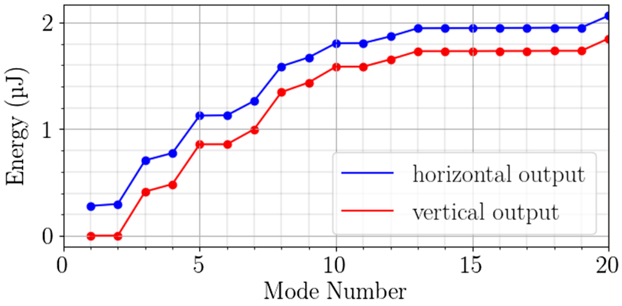

FIG. 20. Cumulative baseline IOM energies for a bunch with 100 μm vertical offset.

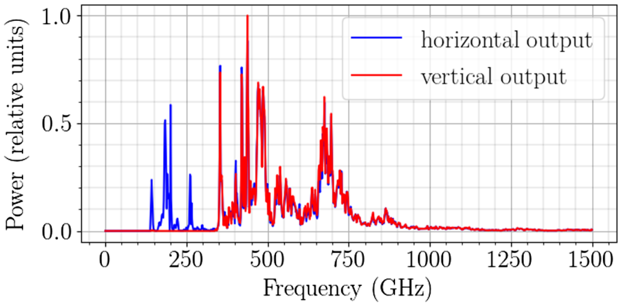

FIG. 21. Baseline IOM energy spectrum for a bunch with 100 μm vertical offset.

V. CONCLUSION

The electromagnetic design of a transition section containing rf output couplers for the TM_{01} and HE_{11} modes of a corrugated waveguide (CWG) module used as a collinear wakefield accelerator (CWA) has been presented. In addition to exhibiting wide bandwidth and high coupling efficiency, the peak fields and pulse heating due to the incident TM_{01} pulse have been shown to be similar to those in the CWG. Extraction of the HE_{11} mode by the TE_{11} IOM coupler has been shown to allow the detection of drive bunch instabilities by providing a measurement of the drive bunch center of charge offset in the CWG. Fabrication of the transition section with above-listed parameters is in progress at the time of writing.

ACKNOWLEDGMENTS

This manuscript is based upon work supported by Laboratory Directed Research and Development (LDRD) funding from Argonne National Laboratory (ANL), provided by the Director, Office of Science, of the U.S. Department of Energy under Contract No. DE-AC02-06CH11357. Useful discussions with S. Lee, A. Nassiri, B. Popovic, S. Sorsher, K. Suthar, E. Trakhtenberg, and J. Xu of ANL are gratefully acknowledged.

APPENDIX: HOM COUPLING

The interaction between the electron bunch and the TM_{01} electromagnetic mode of the CWG is described by the wakefield loss factor κ and form factor F. Here, we show that coupling to HOMs, including the HE_{11} mode, requires a modified version of the form factor which depends on the physical shape of the bunch in addition to the peak current distribution. In the following derivation, we write the current distribution of the bunch in cylindrical coordinates as $J_z(r', \phi', t', t)$. Here, the primed coordinates represent the coordinate system within the bunch with $t' = 0$ at the head of the bunch. The t coordinate is the flight time within the CWA with $t = 0$ at the entrance of the structure. We will assume the shape of the bunch described by J_z varies slowly compared to the temporal length of the bunch l/c. In one dimension, the energy lost by a unit of charge idt' moving a distance cdt in an electric field E_z is

$$d^2U_{\mathrm{loss}} = (idt')(cdt)E_z. \tag{A1}$$

Extending to the continuous current density J_z:

$$d^2U_{\mathrm{loss}} = \int_0^{2\pi}\int_0^{\infty}(J_z dt')(cdt)E_z r' dr' d\phi'. \tag{A2}$$

Here $E_z(r', \phi', t', t)$ is the longitudinal electric field component of the wakefield generated by the leading particles in the bunch. When the corrugation dimensions are small compared to the wavelength of the electromagnetic mode, the corrugated wall can be replaced by an effective surface impedance boundary condition [18]. The x-polarized component of the time harmonic solution for the longitudinal electric field $E_{z,m}$ then takes the form

$$E_{z,m}(r, \phi, z) = J_m(k_r r)\cos(m\phi) f_m(z), \tag{A3}$$

where J_m is the Bessel function of the first kind and order m and the function f_m contains the z dependence of the field. Note that in what follows, the y-polarization follows the same derivation with $\cos(m\phi)$ replaced by $\sin(m\phi)$. Near the center of the structure where $r \to 0$, an approximation of the Bessel function [19] leads to

$$E_{z,m}(r, \phi, z) \approx \frac{1}{m!}\left(\frac{k_r r}{2}\right)^m \cos(m\phi) f_m(z). \tag{A4}$$

Consolidating the constants into the z-dependent function $E_{z0,m}(z)$ leads to

$$E_{z,m}(r, \phi, z) \approx r^m \cos(m\phi) E_{z0,m}(z). \tag{A5}$$

In general, the wakefield loss factor in the CWG is defined as [3]:

$$\kappa = \frac{1}{4U(1-\beta_g)p}\left|\int_0^p E_z e^{jkz} dz\right|^2, \tag{A6}$$

where p is the length of the corrugation unit cell, U is the stored energy, β_g is the normalized group velocity, and k is the wave number of the synchronous mode. This leads to the loss factor $\kappa_m(r, \phi)$ of the mth mode being written as

$$\kappa_m(r, \phi) = \hat{\kappa}_m r^{2m} \cos^2(m\phi) \tag{A7}$$

where $\hat{\kappa}_m$ is defined as

$$\hat{\kappa}_m = \frac{1}{4U(1-\beta_{g,m})p}\left|\int_0^p E_{z0,m}(z) e^{jk_m z} dz\right|^2. \tag{A8}$$

Considering a single mode with synchronous frequency ω, the field induced by a point charge q moving through the structure is $E_z = 2\kappa q \theta(t')\cos(\omega t')$, where $\theta(t')$ is the Heaviside step function. Extending to the continuous current distribution described by J_z, the total $E_z(r, \phi, t', t)$ field is calculated as the convolution integral

$$E_z = \int_{-\infty}^{\infty}\int_0^{2\pi}\int_0^{\infty} 2\hat{\kappa}_m r'^{2m} \cos^2(m\phi') J_z(r', \phi', \tau, t) \times \theta(t'-\tau)\cos\left[\omega(t'-\tau)\right]\frac{r^m \cos(m\phi)}{r'^m \cos(m\phi')} r' dr' d\phi' d\tau. \tag{A9}$$

The fractional term at the end of the integrand of Eq. (A9) is required for normalization since the observation point described by the unprimed coordinates is different from the source point with primed coordinates. We now define

$$g_m(t',t) = \int_0^{2\pi}\int_0^{\infty} r'^m \cos(m\phi')J_z(r',\phi',t',t)r'dr'd\phi', \tag{A10}$$

allowing Eq. (A9) to be written as

$$E_z = 2\hat{\kappa}_m r^m \cos(m\phi)\int_{-\infty}^{\infty} g_m(\tau,t)\theta(t'-\tau) \times \cos(\omega(t'-\tau))d\tau \tag{A11}$$

Inserting (A11) into (A2) and dividing by dt to get the total power flow into the wakefield gives

$$P_w(t) = 2c\hat{\kappa}_m \int_{-\infty}^{\infty} g_m(t',t)\int_{-\infty}^{\infty} g_m(\tau,t) \times \theta(t'-\tau)\cos(\omega[t'-\tau])d\tau dt' \tag{A12}$$

From here, the derivation of the form factor in [3] can be followed, replacing the peak current distribution i by g_m to show that

$$P_w(t) = c\hat{\kappa}_m q_0 |G_m(t)|^2, \tag{A13}$$

where

$$G_m(t) = \frac{1}{q_0}\int_{-\infty}^{\infty} g_m(t',t)e^{-j\omega t'}dt'. \tag{A14}$$

Note that for the TM_{01} monopole mode where $m = 0$, Eq. (A14) reduces to the standard form factor F which is defined in terms of the peak current distribution $i(t')$ alone.

[1] A. Zholents, S. Baturin, D. Doran, W. Jansma, M. Kasa, A. Nassiri, P. Piot, J. Power, A. Siy, S. Sorsher, K. Suthar, W. Tan, E. Trakhtenberg, G. Waldschmidt, and J. Xu, A compact high repetition rate free-electron laser based on the advanced wakefield accelerator technology, in *Proceedings of 11th International Particle Accelerator Conference, IPAC'20, CAEN, France* (2020).

[2] A. Zholents *et al.*, A conceptual design of a compact wakefield accelerator for a high repetition rate multi user x-ray free-electron laser facility, in *Proceedings of 9th International Particle Accelerator Conference, IPAC'18, Vancouver, BC, Canada, 2018* (JACoW, Geneva, Switzerland, 2018), pp. 1266–1268, 10.18429/JACoW-IPAC2018-TUPMF010.

[3] A. Siy, N. Behdad, J. Booske, G. Waldschmidt, and A. Zholents, Design of a cylindrical corrugated waveguide for a collinear wakefield accelerator, Phys. Rev. Accel. Beams **25**, 121601 (2022).

[4] K. L. Bane, P. Chen, and P. B. Wilson, On collinear wakefield acceleration, in *Proceedings of the 11th Particle Accelerator Conference, PAC-1985, Vancouver, BC, Canada, 1985* (IEEE, New York, 1985), Vol. 32, p. 3524.

[5] W. H. Tan, P. Piot, and A. Zholents, Formation of temporally shaped electron bunches for beam-driven collinear wakefield accelerators, Phys. Rev. Accel. Beams **24**, 051303 (2021).

[6] K. Suthar, A. Siy, G. J. Waldschmidt, S. Lee, S. Sorsher, E. Trakhtenberg, and A. Zholents, Determination of maximum repetition rate of a corrugated-waveguide-based wakefield accelerator, in *Proceedings of 11th Mechanical Engineering Design of Synchrotron Radiation Equipment and Instrumentation, MEDSI2020, Chicago, IL* (JACoW, Geneva, Switzerland, 2021), p. 336.

[7] W. K. H. Panofsky and M. Bander, Asymptotic theory of beam break-up in linear accelerators, Rev. Sci. Instrum. **39**, 206 (1968).

[8] V. K. Neil, L. S. Hall, and R. K. Cooper, Further theoretical studies of the beam breakup instability, Part. Accel. **9**, 213 (1979).

[9] A. W. Chao, B. Richter, and C.-Y. Yao, Beam emittance growth caused by transverse deflecting fields in a linear accelerator, Nucl. Instrum. Methods **178**, 1 (1980).

[10] A. Zholents, W. Gai, S. Doran, R. Lindberg, J. G. Power, N. Strelnikov, Y. Sun, E. Trakhtenberg, I. Vasserman, C. Jing, A. Kanareykin, Y. Li, Q. Gao, D. Y. Shchegolkov, and E. I. Simakov, A preliminary design of the collinear dielectric wakefield accelerator, Nucl. Instrum. Methods Phys. Res., Sect. A **829**, 190 (2016).

[11] C. Nantista, S. Tantawi, and V. Dolgashev, Low-field accelerator structure couplers and design techniques, Phys. Rev. ST Accel. Beams **7**, 072001 (2004).

[12] CST Microwave Studio, Dassault Systems, Inc. (2020).

[13] B. Popovic, S. Lee, A. Siy, S. Sorsher, K. Suthar, E. Trakhtenberg, G. J. Waldschmidt, and A. Zholents, Design of miniature waveguides and diamond window assembly for RF extraction and vacuum isolation for the CWA, in *Proceedings of 11th Mechanical Engineering Design of Synchrotron Radiation Equipment and Instrumentation, MEDSI2020, Chicago, IL* (JACoW, Geneva, Switzerland, 2021), Vol. 156.

[14] D. P. Pritzkau and R. H. Siemann, Experimental study of rf pulsed heating on oxygen free electronic copper, Phys. Rev. ST Accel. Beams **5**, 112002 (2002).

[15] D. P. Pritzkau, RF pulsed heating, Ph.D. thesis, SLAC, 2001.

[16] V. E. Balakin, A. V. Novokhatsky, and V. P. Smirnov, VLEPP: Transverse beam dynamics, in *Proceedings of the 12th International Conference on High-Energy Accelerators, HEACC 1983: Fermilab, Batavia, 1983* [*Conf. Proc.* C830811, 119 (1983)].

[17] S. S. Baturin and A. Zholents, Stability condition for the drive bunch in a collinear wakefield accelerator, Phys. Rev. Accel. Beams **21**, 031301 (2018).

[18] G. Stupakov and K. L. Bane, Surface impedance formalism for a metallic beam pipe with small corrugations, Phys. Rev. ST Accel. Beams **15**, 124401 (2012).

[19] Constantine A. Balanis, *Advanced Engineering Electromagnetics (Balanis-1989)*, 2nd ed. (John Wiley and Sons, Hoboken, 1989).